

# Dissociation and faceting of asymmetrical tilt grain boundaries: Molecular dynamics simulations of copper

J. A. Brown\*

*Department of Computational and Data Sciences, MSN 5C3, George Mason University, Fairfax, Virginia 22030, USA*

Y. Mishin†

*Department of Physics and Astronomy, MSN 3F3, George Mason University, Fairfax, Virginia 22030, USA*

(Received 18 June 2007; revised manuscript received 28 August 2007; published 31 October 2007)

Energies and atomic structures of asymmetrical  $\Sigma 11[110]$  tilt grain boundaries in copper have been computed using molecular dynamics with an embedded-atom potential. Two interesting effects have been found: (1) The boundaries dissociate into a low-angle and a high-angle boundary separated by a layer of a fcc-based long-period structure containing intrinsic stacking faults, and (2) the high-energy boundary breaks into nanometer-size facets, some of which are not  $\Sigma 11$  and do not even belong to any coincident-site lattice (CSL). Thus, asymmetrical tilt boundaries locally deviate from the CSL and the average plane imposed by the macroscopic geometry, demonstrating a limitation of the CSL model of grain boundaries. The results are consistent with high-resolution transmission electron microscopy observation available in the literature.

DOI: [10.1103/PhysRevB.76.134118](https://doi.org/10.1103/PhysRevB.76.134118)

PACS number(s): 61.72.Mm, 61.72.Nn, 68.03.Hj, 68.18.Jk

## I. INTRODUCTION

Grain boundaries (GBs), i.e., interfaces between differently oriented crystals of the same material, can play a critical role in many properties of crystalline materials.<sup>1</sup> Most experimental and computer modeling studies of GBs have been focused on so-called symmetrical boundaries, which possess mirror symmetry of crystallographic planes and directions across the boundary plane.<sup>1,2</sup> Consequently, the current understanding of atomic structure and energetics of asymmetrical GBs is far from the level achieved for symmetrical boundaries. This status of the field is not satisfactory for many reasons, including the following.

(i) Most GBs in real polycrystalline materials are asymmetrical.<sup>3-7</sup> In fact, they are often curved and thus sample a range of asymmetrical planes.

(ii) Structures and energies of asymmetrical GBs are required for understanding the phenomenon of GB faceting displayed by many materials.<sup>1</sup> GBs can undergo a spontaneous faceting transition by developing a sawtooth profile composed of atomically flat facets, each having the same lattice misorientation but a different boundary plane.<sup>1,8-10</sup> Faceting transitions are driven by the reduction in the total excess free energy of the crystal<sup>11,12</sup> and often lead to asymmetrical facets even if the average orientation of the GB plane is symmetrical.

(iii) The relative complexity of asymmetrical GBs gives rise to multiplicity of their atomic structures, boundary dissociation processes, nanofaceting, and other fundamentally interesting structural effects, some of which will be addressed in this work. Recent atomistic computer simulations comparing symmetrical and asymmetrical boundaries<sup>13-17</sup> began to uncover a rich variety of possible structures and intriguing structural trends in such boundaries that deserve further investigation.

In this paper, we apply atomistic computer simulations to study  $\Sigma 11[110]$  tilt GBs (tilt angle  $\theta=50.479^\circ$  around the  $[110]$  axis) over the entire range of GB plane inclinations ( $\Sigma$

is the reciprocal density of coincident sites that will be discussed later). It is known from experiment that these GBs exhibit a faceting behavior<sup>8,18-20</sup> and formation of intrinsic stacking faults (ISFs) as part of their structure.<sup>8-10</sup> Since the  $[110]$  zone axis contains two  $\{111\}$  planes, these GBs are convenient for studying the ISF formation process. We choose copper as a model material due to its low ISF energy (which favors the GB dissociation process) and the availability of the well-tested embedded-atom potential<sup>21</sup> describing interatomic bonding in this metal. There are also experimental data on the inclination-angle dependence of the energy of these GBs,<sup>18</sup> which can be used for a cross-check of the calculations.

We will start by discussing the crystallography of the  $\Sigma 11[110]$  tilt GBs and their construction in the computer. After introducing our methodology for finding the ground-state structures and energies of the GBs, we will present a detailed analysis of structural trends across the entire inclination-angle range. This analysis reveals the GB dissociation effect, nanofaceting, and formation of segments of an incommensurate, non- $\Sigma 11$  GB as an integral part of the GB structure. We will also discuss the possible microfaceting of these boundaries and our attempts to observe it by molecular dynamics (MD) simulations. In Sec. VI, we will summarize our findings.

## II. GRAIN BOUNDARY CONSTRUCTION

### A. Simulation block and boundary conditions

We model the GBs using an orthorhombic simulation block with periodic boundary conditions in the  $x$  and  $y$  directions parallel to the boundary plane (Fig. 1). In the normal direction  $z$ , the grains are terminated at free surfaces. This results in an infinitely large slab of the material with a GB in the center and vacuum above and below. In this geometry, the grains are free to translate against each other if this leads to a more favorable GB structure. At the final stage of the

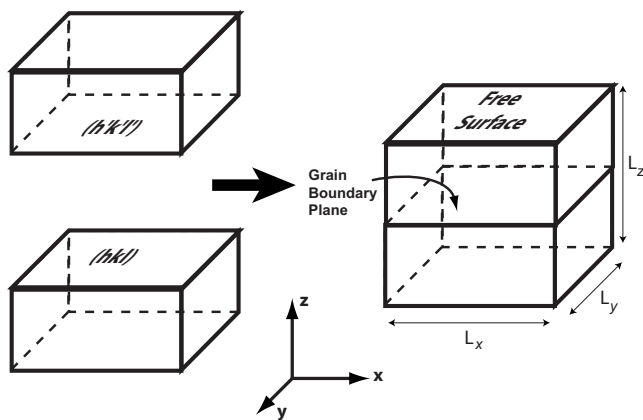


FIG. 1. Geometry of the simulation block used in this work. The grain boundary is created by joining two grains terminated at crystal planes  $(hkl)$  and  $(h'k'l')$ . The boundary is aligned parallel to the  $x$ - $y$  plane of the laboratory coordinate system.

simulations (see details in Sec. III), we fix atomic positions within thin layers adjacent to the surfaces in order to prevent the grain translations.

The slab thickness  $L_z$  (Table I) is large enough to exclude interactions between the GB and the surfaces. This is verified by repeating selected calculations with different thicknesses and checking that the results are nearly the same. The repeat length of the block in the  $y$  direction ( $L_y$ ) is chosen to be 1.53 nm for all boundaries studied here (for the reasons explained later), whereas the repeat length in  $x$  ( $L_x$ ) depends on the particular GB, as indicated in Table I.

### B. Coincident-site lattice boundaries

To prevent long-range elastic strains in the grains, each of the block dimensions  $L_x$  and  $L_y$  in the periodic direction must be a multiple of the common period of the two lattices in that direction. In turn, the existence of a common period requires that the ratio of the lattice periods be a rational number. This

condition is satisfied if the two lattices form a coincident site lattice (CSL) and if the GB plane is chosen to be parallel to a CSL plane.<sup>1</sup> The following geometric constructions have been applied to create asymmetrical CSL boundaries.

Consider two fcc lattices rotated about  $[110]$  by an angle  $\theta$  and allowed to interpenetrate through each other to form a dichromatic pattern. At some angles  $\theta$ , the pattern contains sites shared by both lattices. At such angles, the coincident sites themselves form a lattice, called CSL, which for the  $[110]$  axis is base-centered orthorhombic. The CSL is characterized by the number of sites,  $\Sigma$ , of each lattice per coincident site.

Specifically, Fig. 2 shows the  $\Sigma 11$  CSL produced by a  $\theta = 50.48^\circ$   $[110]$  rotation of two (black and white) fcc lattices. The density of the coincident sites, which are encircled in this figure, is  $1/11$ . The CSL translation vectors in the  $(110)$  plane are  $\vec{b}_1 = \frac{1}{2}[3\bar{3}\bar{2}]$  and  $\vec{b}_2 = [1\bar{1}3]$ , where the Miller indices are given relative to the black lattice and  $\vec{b}_1 \perp \vec{b}_2$ . An arbitrary  $\Sigma 11$   $[110]$  tilt GB can be obtained by aligning the GB plane parallel to a chosen CSL plane containing the  $[110]$  direction and discarding white sites on one side and black sites on the other side of the plane. Note that the dichromatic pattern has mirror symmetry across two of such planes: one is normal to  $\vec{b}_1$  and the other normal to  $\vec{b}_2$ . The choice of these CSL planes as boundary planes produces two well-known symmetrical tilt GBs:  $\Sigma 11$   $(3\bar{3}\bar{2})$   $[110]$  and  $\Sigma 11$   $(1\bar{1}3)$   $[110]$ , respectively.

An asymmetrical boundary is characterized by the *inclination angle*  $\alpha$  between its plane and the  $(3\bar{3}\bar{2})$  plane in the counterclockwise direction. Thus, the two symmetrical GBs correspond to  $\alpha = 0^\circ$  and  $\alpha = 90^\circ$ , respectively. Due to the existence of two perpendicular mirrors, all distinct GB structures are contained within the angular interval  $0 \leq \alpha \leq 90^\circ$ .

A simple way to construct an asymmetrical CSL GB in this angular interval is to choose two non-negative integers,  $i$  and  $j$ , and compose a vector

TABLE I. Properties of selected asymmetrical boundaries.

$\alpha$ ( $^\circ$ )	Plane matching		$\gamma$ ( $J/m^2$ )	$L_x$ (nm)	$L_z$ (nm)
	Upper	Lower			
0	$(\bar{3} 3 2)$	$(3 \bar{3} 2)$	0.702	9.59	12.52
13.26	$(\bar{8} 8 9)$	$(10 \bar{10} 3)$	0.726	7.39	14.50
19.47	$(\bar{5} 5 7)$	$(7 \bar{7} 1)$	0.673	10.17	11.24
29.50	$(\bar{1} 1 2)$	$(19 \bar{19} \bar{2})$	0.671	13.77	10.73
35.26	$(\bar{2} 2 5)$	$(4 \bar{4} \bar{1})$	0.659	8.81	14.41
46.69	$(\bar{3} 3 13)$	$(9 \bar{9} \bar{5})$	0.642	13.98	13.93
60.50	$(\bar{1} 1 19)$	$(1 \bar{1} \bar{1})$	0.570	9.74	17.70
74.21	$(2 \bar{2} 17)$	$(8 \bar{8} \bar{13})$	0.470	8.81	16.52
81.95	$(7 \bar{7} 32)$	$(13 \bar{13} \bar{28})$	0.407	8.54	16.15
90	$(1 \bar{1} 3)$	$(1 \bar{1} \bar{3})$	0.310	1.70	8.41



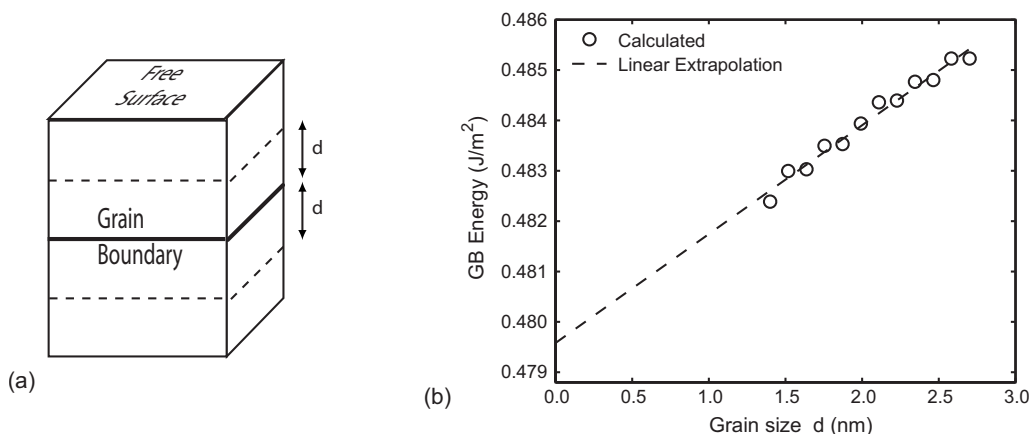


FIG. 4. (a) The grain boundary energy is computed using grain regions of thickness  $d$  adjacent to the boundary. (b). The energy of the incommensurate  $(001)/(1\bar{1}\bar{1})$  boundary is refined by extrapolation to  $d \rightarrow 0$ .

shows that as long as  $\alpha$  is below about  $60^\circ$ , the ISFs are most likely to form in the upper grain, where one of the  $\{111\}$  planes can be almost normal to the boundary plane. In fact, for the  $\alpha=29.5^\circ$  inclination, the  $(1\bar{1}\bar{1})$  plane of the upper grain is exactly normal to the GB, creating the most favorable conditions for the ISF injection. The lower grain has less favorable orientations of the  $\{111\}$  planes. The symmetrical boundaries might also produce ISFs by breaking the mirror symmetry, but they choose not to, as will be discussed later.

Figure 3 also reveals that the  $\{001\}$  plane of each grain is almost (within  $4.3^\circ$ ) parallel to a  $\{111\}$  plane of the other grain. If the GB plane is oriented close to this pair of planes, it may form a facet of the incommensurate  $(001)/(1\bar{1}\bar{1})$  boundary discussed in the previous section, provided this is energetically favorable and the  $4.3^\circ$  misalignment can be accommodated. This scenario is especially plausible when  $\alpha$  approaches  $60.5^\circ$ , the angle at which the  $(1\bar{1}\bar{1})$  plane of the lower grain is exactly parallel to the GB.

These predictions are based on purely geometric considerations and do not include any energetics. They will be tested against atomistic simulation in Sec. IV.

### III. CALCULATION OF BOUNDARY STRUCTURES AND ENERGIES

The embedded-atom potential used in this work accurately reproduces the cohesive energy  $\epsilon_0$ , elastic constants, phonon frequencies, point-defect energies, and other properties of copper.<sup>21</sup> Importantly, it gives the ISF energy  $44.4 \text{ mJ/m}^2$  in very good agreement with experiment.

The ground-state structures of the GBs are determined in three steps. Firstly,  $NVT$  MD is run at temperatures slowly increasing from 0 to 1000 K and then slowly decreasing back to 0 K. During this process, the grains are free to translate past each other in the  $x$  and  $y$  directions and find the most favorable translational state. After repeating such MD runs for a number of different initial grain translations, a configuration with the lowest 0 K energy is identified.

Secondly, the block is created with the most favorable grain translation found at the previous step and MD is run again to verify that the GB remains in that translational state. After that, the surface layers are fixed and the block is relaxed statically at 0 K by minimizing the total potential energy by the conjugate gradient method.

Finally, the relaxed GB structure is tested for an existence of stable structural vacancies.<sup>23</sup> This is accomplished by running semigrand canonical Monte Carlo simulations for a fictitious “binary” system in which the solvent is Cu and the solute is represented by vacancies. Such simulations are run at room temperature with the chemical potential difference between the species equal to  $\epsilon_0$ . If there are sites with a negative vacancy formation energy, this algorithm identifies them and creates vacancies on those sites. If this happens, the structural vacancies can lead to a reconstruction of the GB structure accompanied by a reduction in its excess energy. However, no such vacancies have been found in any of the GBs studied here. This verifies the stability of the ground-state GB structures found in this work against density variations through the removal of atoms. Stability with respect to the addition of atoms (GB interstitials) has not been checked.

Once the GB structure is found, its excess energy  $\gamma$  is determined by selecting lattice regions of equal thickness  $d$  on either side of the boundary [Fig. 4(a)] and computing the total energy  $E$  of this sandwich by summing up the energies of the  $N$  individual atoms it contains (the embedded-atom method partitions the total energy of any atomic configuration into a sum of individual atomic energies<sup>24</sup>). Then,  $\gamma = (E - N\epsilon_0)/A$ , where  $A$  is the GB area.

For the CSL boundaries, this value of  $\gamma$  does not practically depend on the choice of  $d$  as long as the latter is large enough but not too close to the surfaces to avoid interactions with surface atoms. For the incommensurate  $(001)/(1\bar{1}\bar{1})$  GB,  $E$  includes not only the excess GB energy but also the elastic strain energy of the grains. Since the latter contribution is linear in  $d$ , the apparent value of  $\gamma$  must be also linear in  $d$ . This has indeed been verified by the calculations, and the true value of  $\gamma$  has been obtained by extrapolation to  $d \rightarrow 0$  [Fig. 4(b)].

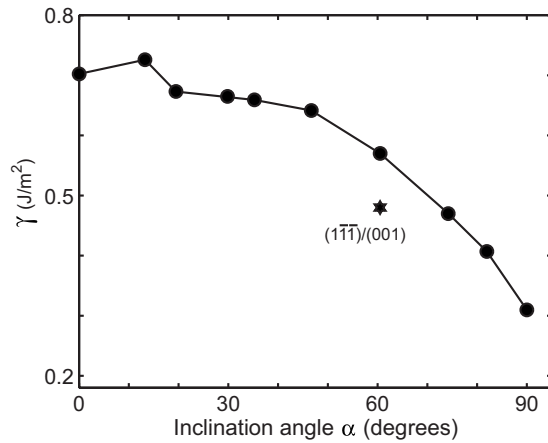


FIG. 5. Calculated energy of  $\Sigma 11$  [110] tilt grain boundaries as a function of the inclination angle  $\alpha$ . The  $(3\bar{3}2)$  and  $(1\bar{1}3)$  symmetrical boundaries correspond to  $\alpha=0$  and  $\alpha=90^\circ$ , respectively. The energy of the incommensurate  $(001)/(1\bar{1}\bar{1})$  boundary is shown for comparison.

#### IV. GRAIN BOUNDARY ENERGIES AND STRUCTURES

##### A. Grain boundary energies

The calculated GB energies are plotted in Fig. 5 versus the inclination angle  $\alpha$ . This plot is in agreement with recent calculations by Tschopp and McDowell<sup>17</sup> using the same embedded-atom Cu potential. The shape of this plot is in reasonable agreement with experiment,<sup>18</sup> especially considering that the experimental GB energies were measured relative to the surface energy whose value and orientation dependence are unknown. The common and striking feature of both the calculated and the experimental angular dependencies is the significant disparity between the two extremes of the symmetrical GBs. Their energies are different by more than a factor of 2 (Table I). It is known from previous work<sup>2,25</sup> that the  $\Sigma 11$   $(1\bar{1}3)$  [110] ( $\alpha=90^\circ$ ) boundary has a particularly low energy among high-angle boundaries in fcc metals, although not quite as low as the  $\Sigma 3$   $(1\bar{1}1)$  [110] coherent twin boundary [ $22 \text{ mJ/m}^2$  in Cu (Ref. 21)]. This low energy is an important factor in the structural trends observed in this set of boundaries.

The additional data point shown in Fig. 5 is for the  $(001)/(1\bar{1}\bar{1})$  GB. Although this boundary is not  $\Sigma 11$ , its tilt angle is only  $4.3^\circ$  away from the  $\Sigma 11$   $(1\bar{1}\bar{1})$  [110] ( $\alpha=60.5^\circ$ ) GB. We therefore plot its energy with the inclination angle  $\alpha=60.5^\circ$ . Note that this energy is significantly lower than for the  $\Sigma 11$  GBs with the same or close inclination angles, suggesting that this boundary might be a good candidate for faceting.

##### B. Grain boundary structures

The GB structures found in this work will be discussed starting from the simplest cases and moving toward more complex. They will be shown as projections along [110], with different symbols indicating atomic positions in alternate (220) planes and with structural units outlined for clarity. In some of the structures, the atoms are represented by spheres whose color depends on the centrosymmetry parameter,<sup>26</sup> the darkest color corresponding to the perfect fcc lattice. This latter format permits a better representation of large-scale features of the boundaries, such as facets and steps.

The atomic structures of the  $\Sigma 11$   $(3\bar{3}2)$  [110] and  $\Sigma 11$   $(1\bar{1}3)$  [110] symmetrical tilt GBs (Fig. 6) are identical to those found in previous work.<sup>13,27–29</sup> While the low-energy  $(1\bar{1}3)$  boundary has a very simple mirror-symmetrical structure consisting of rhombic units, the high-energy  $(3\bar{3}2)$  boundary is more complex, has only a glide symmetry, and is composed of kite-shaped units which represent distorted capped trigonal prisms in a three-dimensional space.

To continue the discussion, a short digression away from the  $\Sigma 11$  misorientation is necessary. Figure 7 shows the structure of the non- $\Sigma 11$   $(001)/(1\bar{1}\bar{1})$  GB mentioned above. It consists of kite-shaped units that normally share a vertex, but some of them share a bond. The shared bonds represent topological defects in the GB structure, which without such defects would be periodic. The units sharing a bond form rows running parallel to [110], which can be interpreted as intrinsic GB dislocations. This quasiperiodic structure is highly dynamic: The dislocations spontaneously wander along the boundary at elevated temperatures. Furthermore,

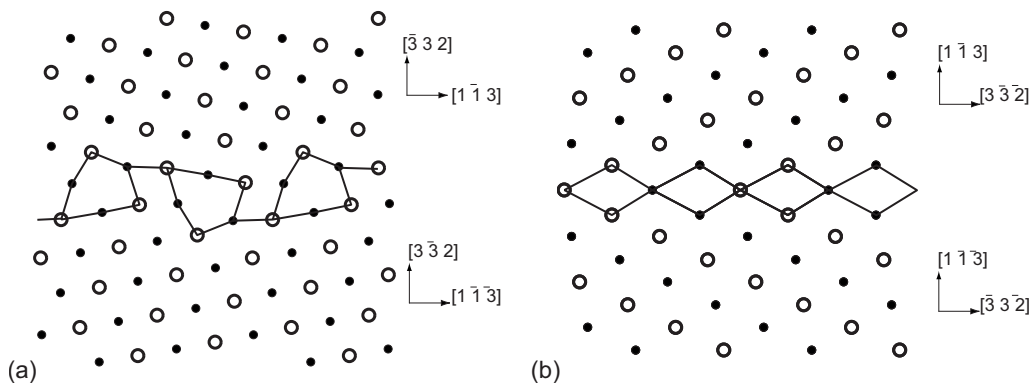


FIG. 6. Atomic structure of the  $\Sigma 11$  [110] symmetrical tilt grain boundaries in copper. (a)  $\alpha=0$  and (b)  $\alpha=90^\circ$ .

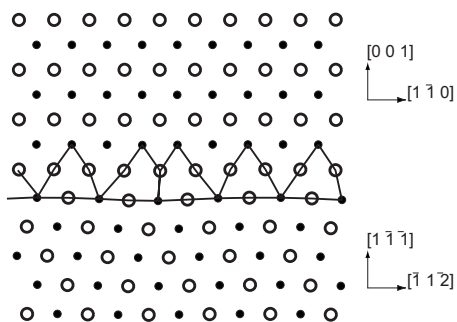


FIG. 7. Atomic structure of the  $(001)/(1\bar{1}\bar{1})$   $[110]$  tilt boundary with the tilt angle  $\theta=54.74^\circ$ . This boundary is incommensurate and has a quasiperiodic structure. It is not a  $\Sigma 11$  boundary.

individual kites can spontaneously move one  $(001)$  layer up (into the upper grain) and then back, thus producing thermal defects (excitations) that turn the initially flat boundary into a relatively rough one. This boundary was studied by high-resolution transmission electron microscopy (HRTEM)<sup>10,30,31</sup> and was found to have a highly localized quasiperiodic structure with short structural units. Our calculations are consistent with those experimental observations as well as with simulations of this boundary in Au.<sup>31</sup>

Returning to the  $\Sigma 11$  boundaries, at inclination angles between approximately  $20^\circ$  and  $70^\circ$ , they develop a periodic array of ISFs extending into the upper grain (Fig. 8). Each ISF terminates at a Shockley partial dislocation in the grain, which under these geometric conditions has a pure edge character.<sup>32</sup> The  $\alpha$  range of the ISF formation and the fact that ISFs extend into the upper grain are consistent with the analysis of crystallographic planes in Sec. II D. The exception is the high-angle end of this range, around  $60^\circ$ – $70^\circ$ , where  $\{111\}$  planes of the lower grain offer a more favorable orientation but the ISFs still form in the upper grain. In this range, the ISF formation process is affected by the nanofaceting, as discussed below. A similar trend for ISFs to extend into one of the grains over the entire inclination range was recently found in  $\Sigma 3$  GBs.<sup>16</sup>

It is important to note that the distance between the ISFs monotonically increases with  $\alpha$ . For example, the stacking sequence of the close-packed planes in the  $\alpha=19.5^\circ$  GB [Fig. 8(a)] is  $\cdots ABCABC|BCABCA \cdots$  with an ISF (denoted by a vertical line) every six planes. The  $\alpha=35.3^\circ$  GB [Fig. 8(c)] has the stacking sequence  $\cdots ABCABCA|CABCABC \cdots$  with an ISF every seven  $\{111\}$  planes. This trend continues until the  $\alpha=74.2^\circ$  GB, in which the ISFs are separated by 15  $\{111\}$  planes [Fig. 8(f)]. Note that the structure of the  $\alpha=29.5^\circ$  GB [Fig. 8(b)] is rather complex and represents a mixture of the neighboring  $\alpha=19.5^\circ$  and  $\alpha=35.3^\circ$  boundaries. Accordingly, the ISF separation alternates between six and seven  $\{111\}$  planes. As expected (Sec. II D), ISF planes are on average normal to the GB.

The formation of ISF arrays can be viewed as a dissociation of the initial  $\Sigma 11$  GB into a low-angle GB formed by the Shockley partials and a high-angle boundary which is no longer  $\Sigma 11$ . Indeed, as the ISFs traverse the lattice regions of the upper grain during the dissociation process, they produce permanent shear deformation and lattice rotation in those

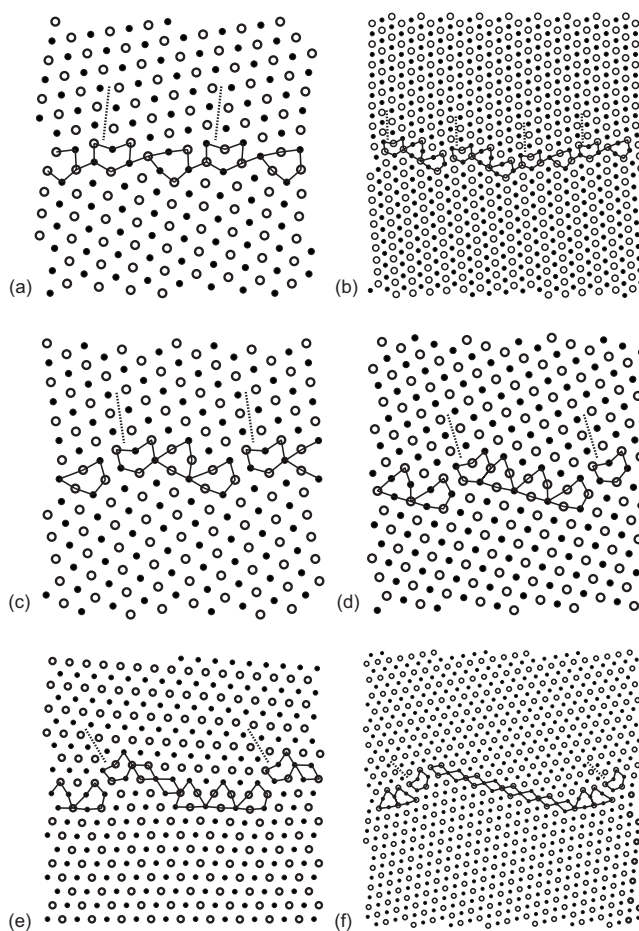


FIG. 8. Atomic structure of selected  $\Sigma 11$   $[110]$  grain boundaries with (a)  $\alpha=19.5^\circ$ , (b)  $\alpha=29.5^\circ$ , (c)  $\alpha=35.3^\circ$ , (d)  $\alpha=46.7^\circ$ , (e)  $\alpha=60.5^\circ$ , and (f)  $\alpha=74.2^\circ$ . The dashed lines outline intrinsic stacking faults extending into the upper grain and terminating at Shockley partial dislocations.

regions. The lattice rotation leads to a local departure of the tilt angle  $\theta$  from the  $\Sigma 11$  misorientation, whereas the shape deformation changes the boundary inclination plane between the ISFs. As a result, the new high-angle boundary produced by the dissociation ends up to be broken into nanofacets whose misorientations are different from  $\Sigma 11$  and whose planes deviate from the average inclination  $\alpha$ .

As long as  $\alpha$  is below about  $50^\circ$ , the atomic structure of the nanofacets between the ISFs is that of the  $(001)/(1\bar{1}\bar{1})$  GB, except that the neighboring kite units share only a vertex [see examples in Figs. 8(b)–8(d)]. Since we do not observe any shared bonds (intrinsic dislocations), which are inevitably present in large areas of this boundary, we conclude that the kites are elastically strained into a periodic array. The  $(001)/(1\bar{1}\bar{1})$  facets are separated by steps, which serve as the initiation sites of the ISFs. Note that each ISF originates from a characteristic structural unit whose shape is different from the familiar rhombic and kite units, although it may be considered as a heavily distorted kite. Such units, which are sometimes referred to as  $E$  units, have been assigned a special role in sliding and other GB properties.<sup>13–17</sup> Each row of such units running parallel to  $[110]$  can be interpreted as the

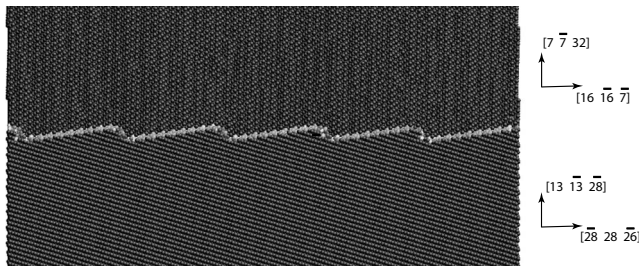


FIG. 9. Nanofaceted structure of the  $\Sigma 11$   $[110]$  grain boundary with  $\alpha=81.95^\circ$ . The long facets represent the  $(1\bar{1}3)$  symmetrical boundary with  $\alpha=90^\circ$ , while the step between the facets contains only one kite-shaped structural unit. The atoms are colored by the centrosymmetry parameter.

core of the trailing Shockley partial dislocation staying in the boundary and bounding the ISF injected into the upper grain.

At  $\alpha > 50^\circ$ , the GBs additionally contain the rhombic units characteristic of the symmetrical  $(1\bar{1}3)$  boundary (Fig. 8). Thus, the boundary now contains two different types of nanofacets. Note that the  $(001)/(1\bar{1}\bar{1})$  facet in the  $\alpha=60.5^\circ$  GB is parallel to the initial GB plane, as expected from our analysis in Sec. II D. As  $\alpha$  increases, the ratio of the areas of the  $(001)/(1\bar{1}\bar{1})$  and  $(1\bar{1}3)$  facets shifts in favor of the latter until the  $(001)/(1\bar{1}\bar{1})$  facet shrinks to two kites [Fig. 8(f)], then to one (Fig. 9), and finally disappears as we arrive at the symmetrical  $(1\bar{1}3)$  boundary ( $\alpha=90^\circ$ ).

## V. MICROFACETING OF ASYMMETRICAL BOUNDARIES

Although the GB structures discussed in the previous section display faceting on the scale of 1–5 nm, the periodic boundary conditions and the relatively small size of the simulation block prevent them from developing facets on a larger scale. Since the energy of these GBs varies very significantly with the inclination angle (Fig. 5), they may form facets also on a scale of 10–100 nm or larger. This type of faceting, which we refer to as microfaceting, is examined in this section.

It is common to analyze faceting of interfaces using the Gibbs-Wulff construction.<sup>1</sup> The interface energy is plotted in polar coordinates, a plane is constructed normal to the radius at each point of the plot, and all points on the outer side of this plane are rejected. The remaining region of space bounded by all such normal planes is called the Wulff shape of the crystal. For interphase boundaries, this gives the equilibrium shape of the crystal, which minimizes the total interface energy under a constant volume. For GBs, the Wulff shape cannot be interpreted as the equilibrium shape of an isolated grain since there is no reason to expect that its volume will be conserved. Nevertheless, this is a useful geometric construction for predicting possible faceting transitions.

Figure 10 shows the polar plot of the calculated GB energy as a function of  $\alpha$ , along with the Wulff shape that results. Based on this shape, faceting can be predicted between the inclination angles of  $30^\circ$ – $90^\circ$ . Any boundary in

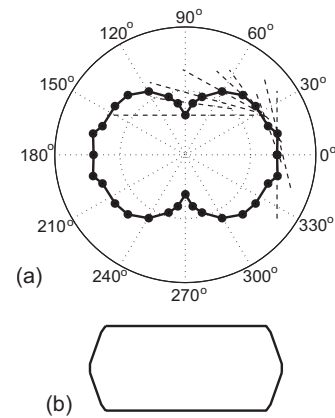


FIG. 10. (a) Polar plot of the calculated  $\Sigma 11$   $[110]$  tilt grain boundary energy in Cu and (b) the corresponding Wulff shape. The dashed lines show some of the normal planes involved in the Gibbs-Wulff construction.

this inclination range should form facets of the low-energy symmetrical  $(1\bar{1}3)$  boundary and an asymmetrical boundary with  $\alpha \approx 30^\circ$ , e.g.,  $\alpha=29.5^\circ$ . In addition, a short facet of the high-energy symmetrical  $(3\bar{3}\bar{2})$  boundary may form at  $\alpha \rightarrow 0$ . When  $\alpha$  is not too small but below  $\sim 30^\circ$ , the boundary should be stable against microfaceting and can be continuously curved. These predictions are generally consistent with the HRTEM observation in Au, which will be discussed in Sec. VI.

Attempts have been made to observe the microfaceting by MD simulations using large simulation blocks (up to 150 000 atoms). The simulated annealing method has been applied in which the temperature is slowly raised to 1000 K, held constant for 2 ns, and then slowly reduced to 0 K, followed by static relaxation. In an attempt to minimize the atomic movements required for faceting, artificially faceted boundaries with the desired average inclination have been created as initial configurations for the simulated anneals. Because the results of these simulations are not completely conclusive due to the limited time scale of MD, only two examples are presented below.

A boundary with an average inclination of  $\alpha=74.21^\circ$  has been constructed using the two symmetrical GBs as the initial facets (Fig. 11). This boundary is expected to shorten the  $\alpha=0$  facet and to develop a continuously curved region between the symmetrical facets, which may look like a corner of the Wulff shape (Fig. 10). After the simulated anneal, the  $\alpha=90^\circ$  facet remains intact, the  $\alpha=0$  facet does indeed shorten, and the boundary develops an intermediate region containing a segment with the  $\alpha=19.5^\circ$  inclination (readily recognizable by the spacing of the ISFs). The latter inclination is expected to be stable and was indeed observed by HRTEM in the corner of an enclosed  $\Sigma 11$  grain in Au.<sup>9</sup> It is not clear, however, how this configuration would evolve should the simulation be continued much longer.

In Fig. 12, the average GB inclination is the same, but the highly energetic  $\alpha=0$  facet is replaced by an  $\alpha=50^\circ$  boundary in the initial configuration. The  $\alpha=50^\circ$  facet is expected to rotate toward  $\alpha \approx 30^\circ$ , thus increasing the angle between

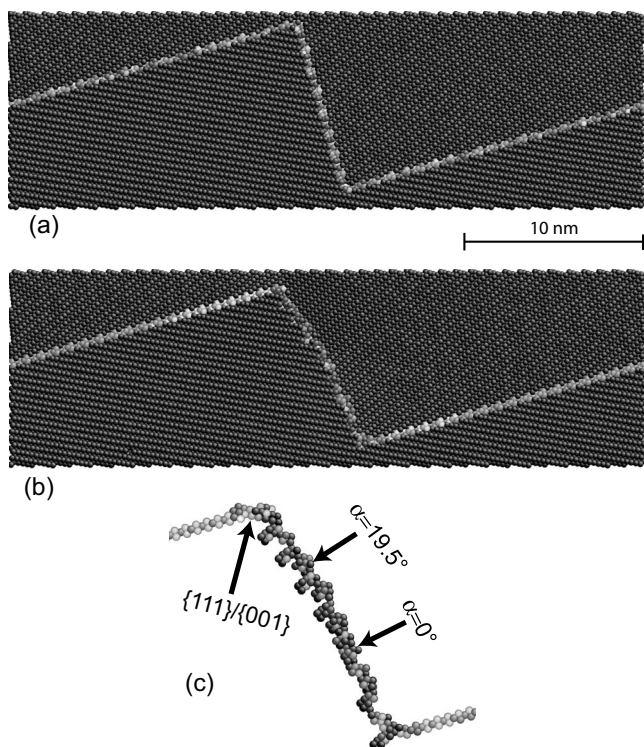


FIG. 11. (a) Initial and (b) final structures of the asymmetrical grain boundary, with the average inclination  $\alpha=74.21^\circ$  relaxed by a simulated anneal. The initial configuration is faceted into the symmetrical boundaries. (c) shows a detailed view of the central facet, with the bulk atoms removed for clarity.

the two facets (the trend which is opposite to the previous example). Again, after the simulated anneal, the  $\alpha=90^\circ$  facet remains unchanged, but rotation of the  $\alpha=50^\circ$  cannot be detected. Instead, it breaks into nanofacets containing  $\alpha=90^\circ$  and  $(001)/(1\bar{1}\bar{1})$  fragments and develops a slight curvature. This configuration is likely to be transient, but further anneals toward equilibrium have not been possible for computational reasons. Note that the driving force of faceting in this case is smaller than in the previous example.

### VI. DISCUSSION AND CONCLUSIONS

We have investigated the atomic structures of copper tilt GBs with the  $\Sigma 11$   $[110]$  tilt misorientation ( $\theta=50.48^\circ$ ) and inclination angles  $\alpha$  covering the entire range of  $0^\circ-90^\circ$ . Although this misorientation and the average GB plane are imposed by the boundary conditions of the simulation block, the relaxed structures of all asymmetrical boundaries reveal local departures from both the  $\Sigma 11$  CSL and the imposed GB plane. Assuming a continuous behavior of the structures between the particular inclination angles tested in this work, the following structural trends can be deduced from the simulations.

The symmetrical GBs arising at  $\alpha=0$  and  $\alpha=90^\circ$  have periodic atomic structures composed of identical structural units and consistent with the CSL model. The asymmetrical boundaries, on the other hand, are always nanofaceted. They

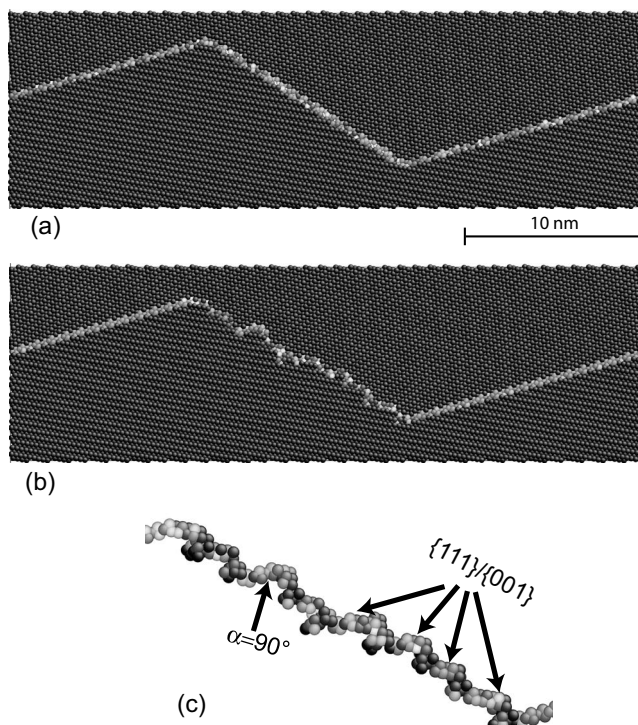


FIG. 12. (a) Initial and (b) final structures of the asymmetrical grain boundary, with the average inclination  $\alpha=74.21^\circ$  relaxed by a simulated anneal. The initial configuration is faceted into the symmetrical  $\alpha=90^\circ$  and asymmetrical  $\alpha=50^\circ$  boundaries. (c) shows a detailed view of the central facet, with the bulk atoms removed for clarity.

form either non- $\Sigma 11$   $(001)/(1\bar{1}\bar{1})$  facets (when  $\alpha < 50^\circ$ ) or pairs of facets representing the  $(001)/(1\bar{1}\bar{1})$  and the symmetrical  $(1\bar{1}\bar{3})$  GBs whose planes are  $18^\circ$  apart (when  $\alpha > 50^\circ$ ). The nanofacets, or their pairs, are separated by steps composed of  $E$  units and bounding ISFs injected into the upper grain. The other end of each ISF is a Shockley partial dislocation inside the grain.

The areas of the facets vary monotonically with  $\alpha$ . At  $\alpha \rightarrow 0$ , the  $(001)/(1\bar{1}\bar{1})$  facet shrinks to a single structural unit and then disappears, while the  $E$  units convert to normal kites and form the structure of the symmetrical  $(3\bar{3}\bar{2})$  boundary. Likewise, at  $\alpha \rightarrow 90^\circ$ , the  $(001)/(1\bar{1}\bar{1})$  facet shrinks to a single kite and then disappears, whereas the  $(1\bar{1}\bar{3})$  facets grow and comprise the  $(1\bar{1}\bar{3})$  symmetrical boundary. Except for the particular  $\alpha=60.5^\circ$  boundary, in which the  $(001)/(1\bar{1}\bar{1})$  facets are parallel to the average GB plane, the facet inclinations are different from  $\alpha$ .

Another view of these structural trends is that the asymmetrical boundaries dissociate into a low-angle GB formed by the Shockley partials and a non- $\Sigma 11$  high-angle GB. The material between these two GBs has a fcc-based long-period structure containing an array of ISFs. This GB dissociation is a generalization of the  $9R$  phase formation predicted by atomistic simulations and observed by HRTEM at  $\Sigma 3$  incoherent twin boundaries in Cu, Ag, and Au.<sup>33-36</sup> While the  $9R$

structure contains an ISF in every third  $\{111\}$  plane, the ISF separations observed in this work are larger and depend on the inclination angle of the boundary. The smallest ISF separation (six  $\{111\}$  planes) and the largest GB dissociation width are found around  $\alpha \approx 20^\circ$  when the ISFs are almost normal to the average boundary plane. At larger inclination angles, the ISF separation increases while the GB dissociation width tends to decrease.

These findings are not fully compatible with the accepted geometric theory of GBs.<sup>1,2</sup> Indeed, a macroscopic description of a GB is normally given by five geometric degrees of freedom.<sup>1</sup> We have examined a trajectory in this five-dimensional space on which three misorientation angles are fixed to impose the  $\Sigma 11$  CSL; one inclination angle is also fixed, and only the second inclination angle ( $\alpha$ ) is varied. This trajectory connects two symmetrical tilt GBs and samples a variety of asymmetrical boundaries in between. The CSL model prescribes that the  $\Sigma 11$  misorientation should be preserved at each point of the GB despite any changes in its inclination angle. Contrary to this, we find that *all* asymmetrical GBs along our trajectory contain nanofacets corresponding to a GB *external* to the trajectory. This  $(001)/(1\bar{1}\bar{1})$  facet is not  $\Sigma 11$  and not even a CSL boundary, but it has a relatively low energy and a tilt angle, which is only  $4.3^\circ$  away from the  $\Sigma 11$  CSL. Thus, the GBs deviate from the trajectory imposed by the macroscopic geometric parameters to incorporate the  $(001)/(1\bar{1}\bar{1})$  facets after slightly straining them to a periodic array of structural units. The energy saving is partially offset by the elastic strain energy associated with these facets and the energy of the ISFs injected into one of the grains to produce the requisite  $4.3^\circ$  lattice rotation. Nevertheless, it is energetically favorable to locally depart from the imposed CSL misorientation or any other CSL in the vicinity of  $\Sigma 11$ . This points to the limited capability of the CSL model to predict the actual structure of asymmetrical GBs. Other limitations of the CSL model have been recently discussed in Ref. 37.

HRTEM studies of Au GBs with misorientations vicinal to  $\Sigma 11$  indicate the formation of ISFs that change the local misorientation by about  $2^\circ$  and permit the formation of exact  $\Sigma 11$  facets with symmetrical inclinations.<sup>10</sup> Such vicinal GBs are also observed to develop  $(001)/(1\bar{1}\bar{1})$  facets in both Au (Ref. 10) and Ni (Ref. 20). The main conclusion of our work is that asymmetrical GBs with even the *exact*  $\Sigma 11$  misorientation imposed in the macroscopic sense *inevitably* de-

velop nanofacets that locally deviate away from the  $\Sigma 11$  or any other CSL, which is accomplished by the ISF mechanism. In some of the GBs studied here, such non-CSL facets alternate with facets of the low-energy symmetrical  $\Sigma 11$  ( $1\bar{1}\bar{3}$ ) GB, thus producing variations of the local misorientation along the boundary.

The Gibbs-Wulff construction based on the computed GB energies suggests that the asymmetrical boundaries should develop faceting on a 10–100 nm or larger scale. Attempts to observe this faceting by MD simulations give results that partially support this prediction but do not always provide convincing evidence. We attribute this to the slow diffusion processes that may be required for the large-scale faceting transformations. They involve generation, diffusion, and annihilation of point defects, the processes which lie beyond the time scale accessible by today's MD simulations.

On the other hand, the faceting predicted by the Wulff construction is very consistent with HRTEM observations of GBs in Au, another metal with a small ISF energy. Figure 8 in Ref. 8 shows an enclosed grain with the  $\Sigma 11$  misorientation, which exhibits mutually perpendicular flat facets corresponding to the symmetrical boundaries connected by relatively smooth regions. A detailed view of one of those regions (Fig. 5 in Ref. 9) reveals  $\alpha = 19.5^\circ$  and  $\alpha = 35.3^\circ$  facets. While the latter is beyond the predicted region of stability against faceting in Cu ( $< 30^\circ$ ), the former is within this range and has indeed been found to be very stable in our simulations.

In the future, it would be interesting to extend this analysis to high-ISF energy metals, such as Al or Ni. The departures from the CSL-predicted structures may still be observed, but the lattice rotation would have to be accommodated by elastic strain or another yet unknown mechanism. The effect of faceting and dissociation on sliding, fracture, and other properties of asymmetrical boundaries is another interesting topic.

#### ACKNOWLEDGMENTS

We are grateful to V. Ivanov for reading the manuscript and making useful suggestions. The atomic configurations shown in Figs. 9, 11, and 12 were visualized using the AtomEye program developed by J. Li (Ref. 38). This work was supported by the U.S. Department of Energy, Office of Basic Energy Sciences, Division of Materials Sciences and Engineering under Contract No. DE-FG02-01ER45871-0006.

\*anthonybrown@ucla.edu

†ymishin@gmu.edu

<sup>1</sup>A. P. Sutton and R. W. Balluffi, *Interfaces in Crystalline Materials* (Clarendon, Oxford, 1995).

<sup>2</sup>*Materials Interfaces: Atomic-Level Structure and Properties*, edited by D. Wolf and S. Yip (Chapman and Hall, London, 1992).

<sup>3</sup>G. S. Rohrer, D. M. Saylor, B. El Dasher, B. L. Adams, A. D. Rollett, and P. Wynblatt, *Z. Metallkd.* **95**, 197 (2004).

<sup>4</sup>D. M. Saylor, A. Morowiec, and G. S. Rohrer, *Acta Mater.* **51**,

3663 (2003).

<sup>5</sup>D. M. Saylor, B. S. El Dasher, A. D. Rollett, and G. S. Rohrer, *Acta Mater.* **52**, 3649 (2004).

<sup>6</sup>C. S. Kim, Y. Hu, G. S. Rohrer, and V. Randle, *Scr. Mater.* **52**, 633 (2005).

<sup>7</sup>C. S. Kim, A. D. Rollett, and G. S. Rohrer, *Scr. Mater.* **54**, 1005 (2006).

<sup>8</sup>K. L. Merkle, *Ultramicroscopy* **37**, 130 (1991).

<sup>9</sup>K. L. Merkle and D. Wolf, *Philos. Mag. A* **65**, 513 (1992).

- <sup>10</sup>K. L. Merkle, *Interface Sci.* **2**, 311 (1995).
- <sup>11</sup>J. W. Cahn, *J. Phys. (Paris)* **43**, 199 (1982).
- <sup>12</sup>J. C. Hamilton, D. J. Siegel, I. Daruka, and F. Léonard, *Phys. Rev. Lett.* **90**, 246102 (2003).
- <sup>13</sup>F. Sansoz and J. F. Molinari, *Acta Mater.* **53**, 1931 (2005).
- <sup>14</sup>D. E. Spearot, M. A. Tschopp, K. I. Jacob, and D. L. McDowell, *Acta Mater.* **55**, 705 (2007).
- <sup>15</sup>M. A. Tschopp, G. J. Tucker, and D. L. McDowell, *Acta Mater.* **55**, 3959 (2007).
- <sup>16</sup>M. A. Tschopp and D. L. McDowell, *Philos. Mag.* **87**, 3147 (2007).
- <sup>17</sup>M. A. Tschopp and D. L. McDowell, *Philos. Mag.* **87**, 3871 (2007).
- <sup>18</sup>N. Goukon, T. Yamada, and M. Kajihara, *Acta Mater.* **48**, 2837 (2000).
- <sup>19</sup>S. B. Lee, *Mater. Lett.* **57**, 3779 (2003).
- <sup>20</sup>O. H. Duparc, S. Poulat, A. Larere, J. Thibault, and L. Priester, *Philos. Mag. A* **80**, 853 (2000).
- <sup>21</sup>Y. Mishin, M. J. Mehl, D. A. Papaconstantopoulos, A. F. Voter, and J. D. Kress, *Phys. Rev. B* **63**, 224106 (2001).
- <sup>22</sup>It can be shown that  $(h'k'l)'$  is  $(3i-2j, 2j-3i, 6j+2i)$  reduced to three smallest integers.
- <sup>23</sup>S. von Althaus, P. D. Haynes, K. Kaski, and A. P. Sutton, *Phys. Rev. Lett.* **96**, 055505 (2006).
- <sup>24</sup>M. S. Daw and M. I. Baskes, *Phys. Rev. B* **29**, 6443 (1984).
- <sup>25</sup>G. Hasson, J. Y. Boos, I. Herbeval, M. Biscondi, and C. Goux, *Surf. Sci.* **31**, 115 (1972).
- <sup>26</sup>C. L. Kelchner, S. J. Plimpton, and J. C. Hamilton, *Phys. Rev. B* **58**, 11085 (1998).
- <sup>27</sup>A. Suzuki and Y. Mishin, *Interface Sci.* **11**, 131 (2003).
- <sup>28</sup>A. Suzuki and Y. Mishin, *Interface Sci.* **11**, 425 (2003).
- <sup>29</sup>J. D. Rittner and D. N. Seidman, *Phys. Rev. B* **54**, 6999 (1996).
- <sup>30</sup>K. L. Merkle, *J. Phys. (Paris)* **51**, C1 (1990).
- <sup>31</sup>K. L. Merkle and D. Wolf, *Mater. Lett.* **17**, 217 (1993).
- <sup>32</sup>The  $1/6\langle 211 \rangle$  Burgers vector of these dislocations has been verified by the standard Burgers circuit construction.
- <sup>33</sup>G. H. Campbell, D. K. Chan, D. L. Medlin, J. E. Anelo, and C. B. Carter, *Scr. Mater.* **35**, 837 (1996).
- <sup>34</sup>F. Ernst, M. W. Finnis, D. Hofmann, T. Muschik, U. Schonberger, U. Wolf, and M. Methfessel, *Phys. Rev. Lett.* **69**, 620 (1992).
- <sup>35</sup>D. L. Medlin, G. H. Campbell, and C. B. Carter, *Acta Mater.* **46**, 5135 (1998).
- <sup>36</sup>D. L. Medlin, S. M. Foiles, and D. Cohen, *Acta Mater.* **49**, 3689 (2001).
- <sup>37</sup>L. A. Bendersky and J. W. Cahn, *J. Mater. Sci.* **41**, 7683 (2006).
- <sup>38</sup>J. Li, *Modell. Simul. Mater. Sci. Eng.* **11**, 173 (2003).